

Investigation of point and extended defects in electron irradiated silicon—Dependence on the particle energy

R. Radu,^{1,a)} I. Pintilie,^{1,a)} L. C. Nistor,¹ E. Fretwurst,² G. Lindstroem,² and L. F. Makarenko³

¹National Institute of Materials Physics, Atomistilor 105 bis, Magurele 077125, Romania

²Institute for Experimental Physics, University of Hamburg, D-22761 Hamburg, Germany

³Belarusian State University, Independence Ave. 4, 220030 Minsk, Belarus

(Received 15 January 2015; accepted 11 April 2015; published online 27 April 2015)

This work is focusing on generation, time evolution, and impact on the electrical performance of silicon diodes impaired by radiation induced active defects. n-type silicon diodes had been irradiated with electrons ranging from 1.5 MeV to 27 MeV. It is shown that the formation of small clusters starts already after irradiation with high fluence of 1.5 MeV electrons. An increase of the introduction rates of both point defects and small clusters with increasing energy is seen, showing saturation for electron energies above \sim 15 MeV. The changes in the leakage current at low irradiation fluence-values proved to be determined by the change in the configuration of the tri-vacancy (V_3). Similar to V_3 , other cluster related defects are showing bistability indicating that they might be associated with larger vacancy clusters. The change of the space charge density with irradiation and with annealing time after irradiation is fully described by accounting for the radiation induced trapping centers. High resolution electron microscopy investigations correlated with the annealing experiments revealed changes in the spatial structure of the defects. Furthermore, it is shown that while the generation of point defects is well described by the classical Non Ionizing Energy Loss (NIEL), the formation of small defect clusters is better described by the “effective NIEL” using results from molecular dynamics simulations. © 2015 Author(s). All article content, except where otherwise noted, is licensed under a Creative Commons Attribution 3.0 Unported License.

[<http://dx.doi.org/10.1063/1.4918924>]

I. INTRODUCTION

The present work had been largely triggered by the challenge presented by the Large Hadron Collider (LHC) at the European Nuclear Research Centre CERN and its planned High Luminosity upgrade (HL-LHC) foreseen now to start in 2020.¹ Silicon detectors are increasingly in use for various applications in fundamental research such as elementary particle and nuclear physics and research with photons or radiation in free electron laser experiments.² The main reason for the extended use of these detectors is the unique flexibility of their structural design for extreme high spatial and time resolution with high signal to noise ratio, the possibility for electronic integration on the same chip, and the large experience in semiconductor process technology. However, the impact of the large particle intensity by charged hadrons leads to radiation damage effects in the silicon material and hence to degradation in the detector performance limiting their practical use. Any promising attempt for radiation hardening of the silicon material as well as improvements by modifying the detector processing will rely on a thorough knowledge of the generation of electrically active defects in the bulk material. Macroscopic effects induced by irradiation in silicon detectors as seen from the device electrical characteristics measured at room temperature (RT) are:^{3–10} (i) Strong increase of the detector leakage current (LC). This fact requires cooling to cope with the otherwise unavoidable

heating due to the dissipation power in large area installations thus to ensure a tolerable signal/noise ratio for the detection of minimum ionizing particles. (ii) Change of the space charge concentration (N_{eff} —effective doping) and thus of the depletion voltage leading to an apparent type inversion. (iii) Considerable reduction of Charge Collection Efficiency (CCE). An increased charge carrier trapping reduces the signal obtained from a traversing particle and hence affects the signal to noise ratio. These “macroscopic” damage effects are not only depending on the irradiation fluence but are even susceptible to considerable changes during long term storage after irradiation (annealing effects). Both beneficial annealing (during short time after irradiation) and detrimental-annealing effects (during long time storage) are observed, which would either reduce, respectively, increase the originally observed damage effects. This is of extreme importance envisioning a total operation period of 10 and 5 years for the LHC and HL-LHC experiments, respectively. Among the multitude of radiation induced electrically active defects^{10–34} only some proved to have a direct impact on the “macroscopic” behavior of the sensors operating at ambient temperatures. These point- or extended-defects are labeled in the literature as: I_p—a deep acceptor strongly generated in oxygen lean, standard float-zone material (STFZ)^{22–24} and BD—a bistable thermal donor (TDD2)^{24,26,27} strongly generated in oxygen rich float-zone material (DOFZ), both associated with point defects that are stable at room temperature and determining the N_{eff} in silicon diodes irradiated with Co⁶⁰ g-rays; E(30K)—a shallow donor contributing to the

^{a)}R. Radu and I. Pintilie contributed equally to this work.



beneficial annealing after hadron irradiation, strongly generated in diodes irradiated with charged particles;^{10,29} H(116K), H(140K), H(152K)—cluster-related hole traps with enhanced field emission (acceptors in the lower part of the Si bandgap), contributing fully with their concentration to N_{eff} and causing the long term annealing effects (reverse annealing) in hadron irradiated silicon diodes;^{10,29} the bistable E4 and E5 energy levels—identified with the double and single acceptor charge state of the V₃ defect in a configuration part of a hexagonal ring (PHR), respectively,^{30–33} a defect contributing to the magnitude of the leakage current in the Si sensors and bipolar transistors upon irradiation with high energy particles.^{28,31} The most important characteristics of these defects, including some features resulted from the present work, are summarized in Table I. The present work is focusing on generation and annealing of the defects having a direct influence on the device characteristics. The radiation damage for the above mentioned applications is primarily due to bulk damage, consisting in the generation of isolated point- and extended cluster defects. As point defects are produced by low energy silicon recoils, cluster effects are due to larger energy recoils which will then lead to a dense cascade of silicon atoms removed from their specific lattice sites. For investigating the generation process of point and extended defects, we have used irradiation by mono-energetic electrons in a wide energy range from 1.5 to 27 MeV.

II. EXPERIMENTAL DETAILS

A. Samples

The studies presented in this work are performed on three types of n-type silicon crystals with a (100) orientation: (i) STFZ, (ii) DOFZ, and (iii) n-type epitaxial silicon layer (EPI) grown on a Czochralski substrate. The thickness of the p⁺-n-n⁺ planar pad diodes is 280 μm for float-zone materials (STFZ and DOFZ) and 50 μm for EPI silicon. The doping concentration is N_d = 8 × 10¹¹ cm⁻³ in float-zone samples and N_d = 6 × 10¹³ cm⁻³ in EPI material. For all samples (26 in total), the areas of the front (p⁺) and back (n⁺) contacts are 5 × 5 mm² and 10 × 10 mm², respectively. The oxygen enrichment for the DOFZ process was achieved by a 72 h post-oxidation O diffusion at 1150 °C resulting in an average oxygen concentration of 1.2 × 10¹⁷ cm⁻³, ~20 times larger than in the STFZ ones.¹⁰ The oxygen content in EPI diodes is 2 × 10¹⁷ cm⁻³, similar to the DOFZ samples. The Carbon content in all of the investigated materials is ~2 × 10¹⁵ cm⁻³.¹⁰

B. Irradiations

These samples were irradiated with electrons with energies of 1.5 MeV, 3.5 MeV, 6 MeV, 15 MeV, and 27 MeV and fluence values ranging from 5 × 10¹¹ cm⁻² to 2 × 10¹⁶ cm⁻² using different irradiation facilities: with 1.5 MeV electrons at the Energy and Nuclear Research Institute (IPEN-CNEN/SP), Sao Paolo, Brazil,³⁵ with 3.5 MeV electrons at the Belarusian State University, Belarus,³⁶ with 6 MeV and 27 MeV electrons at the Metrology Institute PTB, Braunschweig, Germany,³⁷ and with 15 MeV electrons at

the ELBE facility at the Helmholtz-Zentrum Dresden-Rossendorf, Germany.³⁸

C. Characterization

The irradiated samples have been characterized primarily by means of Capacitance-Voltage (CV) and Current-Voltage (IV) characteristics at 20 °C. For all the samples, the CV measurements are performed with an ac small signal of 0.5 V and frequency of 10 kHz. Investigations of electrically active defects induced by irradiation have been performed by Deep Level Transient Spectroscopy (DLTS) and Thermally Stimulated Current (TSC) techniques, on samples with the guard ring grounded. This procedure is required for an accurate determination of the trap concentrations.^{26,39} For all the TSC measurements, the filling of the traps was performed at 10 K with a forward current of 2 mA (reachable by applying a forward bias usually larger than 10 V) for 30 s. The heating rate used to record the TSC spectra was 11 K/min. Saturation of the TSC peaks was obtained for reverse biases of V_R ≥ 200 V applied during heating. For the investigation of the annealing process with the DLTS and TSC techniques, an isothermal heat treatment at 80 °C was chosen to accelerate the process with respect to room temperature. This isothermal study is the common procedure in the CERN-RD50 community^{3–6} for comparison with other experiments. The formation of the extended defects and the change in their spatial structure during annealing experiments was investigated by High Resolution Transmission Electron Microscopy (HRTEM). The microstructure investigation has been carried out on cross-section specimens with the JEOL JEM-ARM/200F field emission atomic resolution analytical electron microscope operating at 200 kV. Cross section TEM specimens have been prepared in the conventional way by sawing the specimens, gluing the pieces film to film, mechanical thinning with the tripod, followed by ion milling using the Gatan PIPS machine.

D. Impact of defects on the device electrical characteristics

According to the trapping parameters (energy position of the defect level in the bandgap of the semiconductor material E_t , capture cross section for electrons σ_n and for holes σ_p) and concentration (N_t), and by neglecting the concentration of free carriers in the depleted region of the diode, the change in the leakage current in stationary conditions at a certain temperature (T) caused by a certain defect can be estimated based on Shockley-Read-Hall statistics as^{40–42}

$$\Delta LC(T) = q \times A \times d \times N_t \frac{e_n(T)e_p(T)}{e_n(T) + e_p(T)}, \quad \text{with} \\ e_n(T) = v_{th,n}(T) \times \sigma_n(T) \times N_C \times \exp\left(-\frac{E_c - E_t}{k_B T}\right), \quad (1) \\ e_p(T) = v_{th,p}(T) \times \sigma_p(T) \times N_V \times \exp\left(-\frac{E_t - E_V}{k_B T}\right),$$

where q is the elementary charge, A is the area of the diode, d is the diode thickness, $v_{th,n,p}$ are the thermal velocities of

TABLE I. Electrical properties of point and extended defects relevant for detector operation.

Defect label	Assignment and particularities	Configurations and charge states	Energy levels (eV) and capture cross sections (cm^2)	Impact on electrical characteristics of Si diodes at RT
E(30 K)	Not identified extended defect. Donor with energy level in the upper part of the bandgap, strongly generated by irradiation with charged particles ^{10,29} Linear fluence dependence (this work)	$\text{E}(30 \text{ K})^{0/+}$	$E_c - 0.1 \sigma_n = 2.3 \times 10^{-14}$	Contributes in full concentration with positive space charge to N_{eff}
BD	<i>TDD2</i> —point defect Bistable donor existing in two configurations (A and B) with energy levels in the upper part of the bandgap, strongly generated in Oxygen rich material ^{24,26,27}	$\text{BD}_A^{0/++}$ $\text{BD}_B^{+/++}$	$E_c - 0.225 \sigma_n = 2.3 \times 10^{-14}$ $E_c - 0.15 \sigma_n = 2.7 \times 10^{-12}$	It contributes twice with its full concentration with positive space charge to N_{eff} , in both of the configurations
I_p	Not identified point defect. Suggestions: V_2O or a Carbon related center ^{10,22–24} Amphoteric defect generated via a second order process (quadratic fluence dependence), strongly generated in Oxygen lean material ^{22–24} (this work)	$I_p^{+/0}$ $I_p^{0/-}$	$E_V + 0.23 \sigma_p = (0.5–9) \times 10^{-15}$ $E_c - 0.545 \sigma_n = 1.7 \times 10^{-15}$ $\sigma_p = 9 \times 10^{-14}$	No impact Contributes to both N_{eff} and LC
E ₇₅	<i>Tri-vacancy (V_3)</i> —small cluster	$\text{FFCV}_3^{-/0}$	$E_c - 0.075 \text{ eV } \sigma_n = 3.7 \times 10^{-15}$	No impact
E ₄	<i>Bistable defect</i> existing in two configurations (FFC and PHR) with acceptor energy levels in the upper part of the bandgap ^{10,28,30–33} Linear fluence dependence (this work)	$\text{PHRV}_3^{=/-}$	$E_c - 0.359 \sigma_n = 2.15 \times 10^{-15}$	No impact
E ₅		$\text{PHRV}_3^{-/0}$	$E_c - 0.458 \sigma_n = 2.4 \times 10^{-15}$ $\sigma_p = 2.15 \times 10^{-13}$	Contributes to LC
H(116 K)	Not identified extended defect. Acceptor with energy level in the lower part of the bandgap ^{10,29} Linear fluence dependence (this work)	$\text{H}(116 \text{ K})^{0/-}$	$E_V + 0.33 \sigma_p = 4 \times 10^{-14}$	Contributes in full concentration with negative space charge to N_{eff}
H(140 K)	Not identified extended defect. Acceptor with energy level in the lower part of the bandgap ^{10,29} Linear fluence dependence (this work)	$\text{H}(140 \text{ K})^{0/-}$	$E_V + 0.36 \sigma_p = 2.5 \times 10^{-15}$	Contributes in full concentration with negative space charge to N_{eff}
H(152 K)	Not identified extended defect. Acceptor with energy level in the lower part of the bandgap ^{10,29} Linear fluence dependence (this work)	$\text{H}(152 \text{ K})^{0/-}$	$E_V + 0.42 \sigma_p = 2.3 \times 10^{-14}$	Contributes in full concentration with negative space charge to N_{eff}

electrons (n) or holes (p), $N_{C,V}$ are the effective density of states in the conduction/valence band, and E_C and E_V are the conduction and valence band edge energies, respectively.

Depending on the charge state of the defect (acceptors $-/0$ or donors $+/0$), the change in the effective doping concentration in an n-type diode, under stationary conditions, can be estimated according to the steady state occupancy of the defect (n_t —when occupied by electrons and p_t when occupied by holes)

$$\begin{aligned}\Delta N_{\text{eff}}^{\text{acceptor}}(T) &= -n_t^{\text{acceptor}}(T) = -N_t^{\text{acceptor}} \frac{e_p(T)}{e_n(T) + e_p(T)}, \\ \Delta N_{\text{eff}}^{\text{donor}}(T) &= +p_t^{\text{donor}}(T) = +N_t^{\text{donor}} \frac{e_n(T)}{e_n(T) + e_p(T)}.\end{aligned}\quad (2)$$

When more defects are involved the resulting effective doping concentration can be estimated by

$$N_{\text{eff}}(T) = N_d + \sum_i p_{t,i}^{\text{donor}}(T) - \sum_j n_{t,j}^{\text{acceptor}}(T). \quad (3)$$

It is worth noting that in order to determine the influence of the defects on the electrical characteristics of the device both capture cross sections (σ_n and σ_p) have to be known. This is important for defects with energy levels close to the midgap when the emission rates e_n and e_p may be comparable and hence none of them can be neglected.

III. DEFECT INVESTIGATIONS

A. Electrical characterization: Generation rates, annealing, and impact on the device characteristics

As mentioned above, the defect formation, from point defects to clusters, is scanned in this work by performing irradiation with electrons of five different energies ranging from 1.5 MeV to 27 MeV. The samples irradiated with low fluence were investigated by means of DLTS technique, while TSC experiments were employed for highly irradiated diodes. The DLTS spectra recorded after irradiation of an EPI diode with 1.5 MeV electrons, fluence $\Phi = 1.75 \times 10^{14} \text{ cm}^{-2}$, are shown in Fig. 1.

One can observe that all the detected DLTS peaks are associated only with the well-known point defects, namely, VO_i , C_iO_i , and V_2 (in the two acceptor charge states). Thus, the main damage caused by irradiation with low fluence of 1.5 MeV electrons is due to the generation of point defects only, originating from primary-generated interstitials and vacancies that are mobile at room temperature.

This is similar to the case of irradiations with Co^{60} - γ -rays of STFZ and DOFZ diodes.²⁴ Low fluence irradiations with electrons of larger energies reveal the generation of small clusters of tri-vacancies (V_3) in PHR configuration. In this planar configuration, the V_3 defect has two energy levels, corresponding to double and single acceptor states at 0.359 eV and 0.458 eV below the conduction band of silicon.³⁰ Examples of DLTS spectra recorded after irradiation with electrons of 3.5 MeV and 27 MeV are shown in Fig. 2.

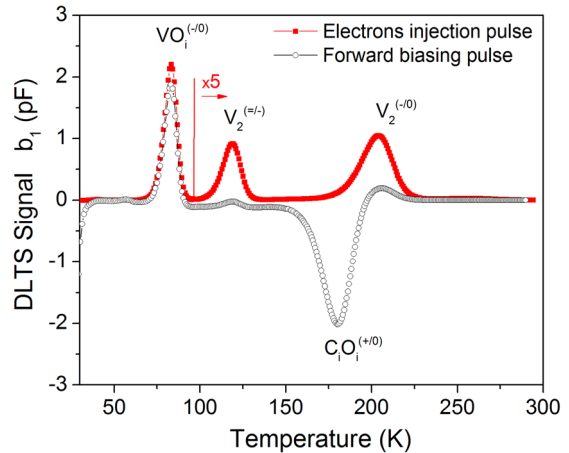


FIG. 1. DLTS spectra measured on an EPI diode, irradiated with 1.5 MeV electrons ($\Phi = 1.75 \times 10^{14} \text{ cm}^{-2}$), after electron injection (filled symbols) and forward biasing (open symbols). Measurements done with: reverse bias $U_R = -20 \text{ V}$, voltage pulse for electrons injection $U_{P,e} = -0.1 \text{ V}$, forward voltage pulse for bipolar injection $U_{P,Fw} = 3 \text{ V}$, pulse width $t_P = 100 \text{ ms}$, and time window $T_w = 200 \text{ ms}$.

Thus, starting with electrons of 3.5 MeV, the recoil energy is sufficiently high to knock out secondary atoms frequently.

The fluence dependence of VO , V_2 , and V_3 defects detected in these DLTS studies is linear as can be observed from the fits shown in Fig. 3(a) (example given for the irradiations with 3.5 MeV and 15 MeV electrons). The defect concentrations were extracted from the DLTS spectra measured on as irradiated samples. The fits in the log-log scale are done by fixing the slope to 1 (in a linear x-y scale this corresponds to a linear fit with intercept at 0). For the defect concentrations showing a linear fluence dependence, the introduction rates, known also as generation rates, can be calculated as the ratio between the defect concentration and irradiation fluence for different electron energies. For the VO , V_2 , and V_3 (in PHR configuration) defects the introduction rates as function of the electron energy are shown in Fig. 3(b). For the irradiations with low energy electrons, the introduction rates of V_2 and V_3 (PHR) can be readily determined by analyzing the electron emission from the double charge states, that are better separated in temperature than the defects single acceptor states. However, for the irradiations with high energy electrons (starting with 15 MeV), the signals from $\text{V}_2^{(=/-)}$ and $\text{V}_3^{(=/-)}$ start to be reduced by clustering effects as it has been observed previously for the V_2 in ion implanted and hadron damaged diodes.^{10,17} For the irradiations with 15 and 27 MeV, the introduction rates were calculated based on the results given by the fit of the DLTS peak corresponding to the emission from the single charge states of V_2 and V_3 (PHR) as shown in Fig. 2(c). The concentration of V_2 was estimated from the DLTS spectra measured after annealing out of the V_3 (PHR). The concentration of V_3 (PHR) was then determined from the DLTS spectra measured on as-irradiated samples after subtracting the contribution of V_2 .

The increase of the introduction rates of the single vacancies, di-vacancies (also suggested by Corbett⁴³), and tri-vacancies seems to have a saturation behavior for energies higher than 15 MeV, in agreement with the results of

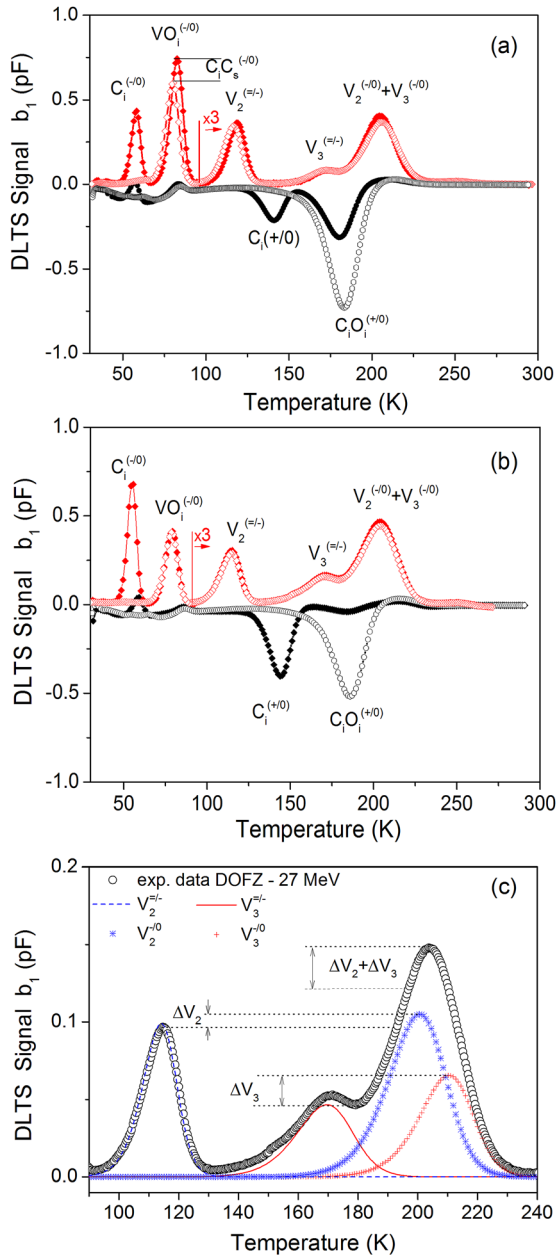


FIG. 2. DLTS spectra measured on DOFZ (open symbols) and STFZ (filled symbols) diodes after irradiation with: (a) 3.5 MeV electrons, $\Phi_{\text{DOFZ}} = 1.7 \times 10^{12} \text{ cm}^{-2}$, $\Phi_{\text{STFZ}} = 1.95 \times 10^{12} \text{ cm}^{-2}$; (b) 27 MeV, $\Phi_{\text{DOFZ}} = 7.1 \times 10^{11} \text{ cm}^{-2}$, $\Phi_{\text{STFZ}} = 7.5 \times 10^{11} \text{ cm}^{-2}$; (c) 27 MeV, $\Phi_{\text{DOFZ}} = 7.1 \times 10^{11} \text{ cm}^{-2}$, clustering effect reflected in different magnitudes of the DLTS peaks for the double and single charged states of V_2 and V_3 defects. The positive spectra correspond to electron injection pulses and the negative ones to pulses of forward biasing. Measurements done with: $U_R = -10 \text{ V}$, $U_{P,e} = -0.1 \text{ V}$, $U_{P,Fw} = 3 \text{ V}$, $t_p = 100 \text{ ms}$, and $T_w = 200 \text{ ms}$.

Wood *et al.*⁴⁴ showing that primary knock on atoms (PKA's) above 12 keV are converting into lower-energy sub-cascades and point defects.

Annealing studies at moderate temperatures (80°C) enable to predict the long term evolution of defects at room temperature,⁴⁵ and the changes in the detector performances if the parameters of the annealing process are known. Thus, Fig. 4(a) shows the isothermal annealing at 80°C of a DOFZ diode irradiated with 6 MeV electrons. The spectrum in the range 95 K to 300 K is magnified by a factor of 3. It has been

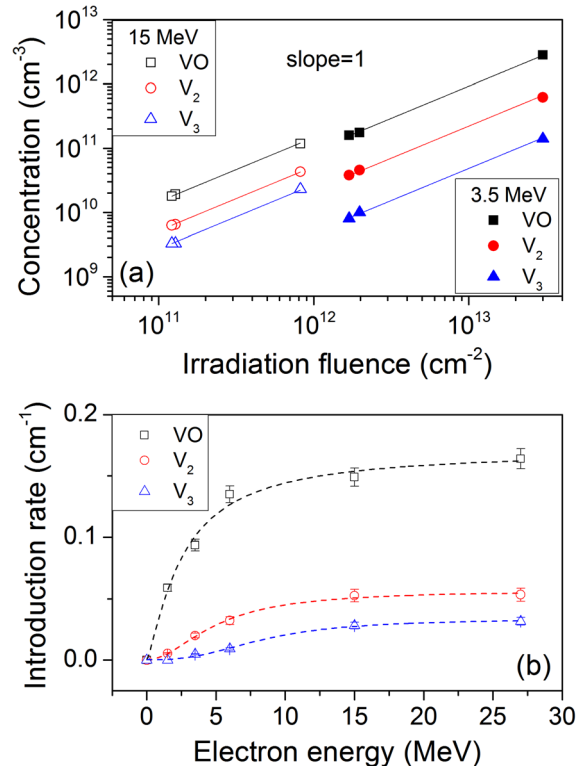


FIG. 3. (a) Fluence dependence of VO , V_2 , and V_3 defects—example of linear fits for samples irradiated with different fluences of 3.5 MeV and 15 MeV electrons. The fit with fixed slope 1 gives correlator coefficients larger than 0.99. (b) Introduction rates for VO , V_2 , and V_3 defects as function of electron energy.

shown previously^{28,30} that the defects explaining the main part of the leakage current are the tri-vacancies $V_3^{(-/0)}$ (also known as a cluster-related defect).

As shown in the literature, this defect is bi-stable, changing its configuration at ambient temperatures from a PHR configuration to a fourfold coordinated (FFC) one,³⁰ while it is stable up to 220°C .^{32,33} It has been shown previously that the recovery of both DLTS signals (from $V_3^{=/-}$ and $V_3^{(-/0)}$) is possible by injection of a high forward current (1 A at 20°C for 10 min).^{28,30,31} If the V_3 defect is partly responsible for the leakage current, then both the leakage current and the defect concentration should have also a similar annealing behavior. Fig. 4(b) shows a comparison between the measured leakage current (open symbols) and the V_3 defect concentration (filled symbols). The leakage current at full depletion was extracted from the I-V measurements at 20°C .

As depicted in Fig. 4(b), the time constants for the annealing at 80°C of the leakage current and of the concentration of V_3 defects in planar configuration (PHR) are very similar, $\tau = (44 \pm 3) \text{ min}$ for LC and $\tau = (43 \pm 2) \text{ min}$ for V_3 . These experiments indicate that the variation seen in the leakage current is entirely related to the change in the concentration of V_3 in PHR configuration. In particular, a direct connection between the V_3 concentration and the leakage current via the $V_3^{(-/0)}$ is plausible as the energy level is located close to the middle of the band gap, and thus may constitute an effective generation center. The energy and the electron capture cross section for this defect level are known to be 0.458 eV below E_C and $\sigma_n = 2.4 \times 10^{-15} \text{ cm}^2$, respectively.³⁰

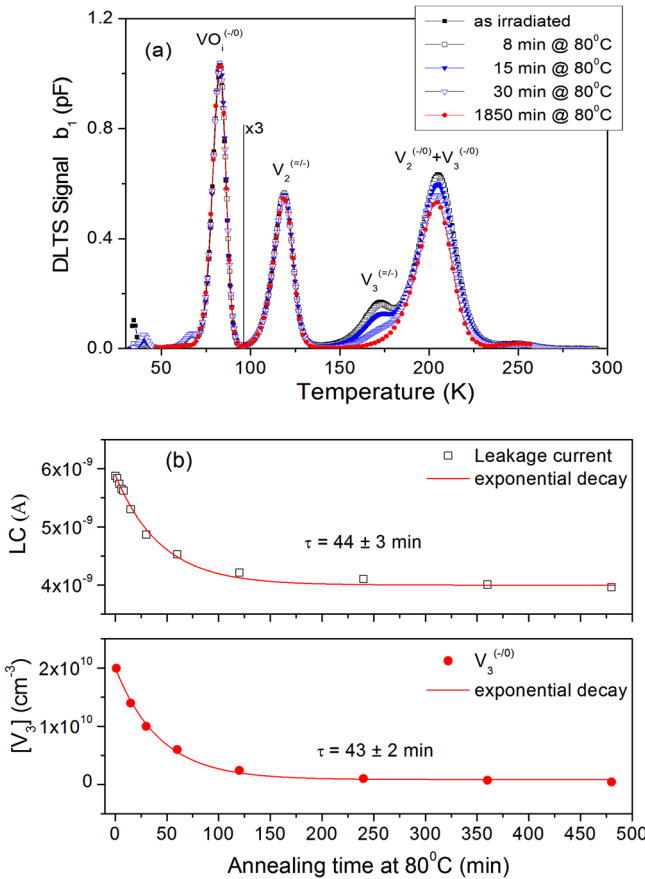


FIG. 4. (a) Isothermal annealing at 80 °C of a DOFZ diode irradiated with 6 MeV electrons with a fluence of $\Phi = 1.55 \times 10^{12} \text{ cm}^{-2}$. Measurements were done with: $U_R = -10 \text{ V}$, $t_p = 100 \text{ ms}$, $T_W = 200 \text{ ms}$, and $U_P = -0.1 \text{ V}$. (b) Annealing behavior of the concentration of the V_3 defects in PHR configuration and of the leakage current measured at 20 °C.

Using these trapping parameters in Eq. (1) as well as the experimental values obtained for the change in the leakage current and in the V_3 concentration, the capture cross section for holes of the $V_3^{(-/0)}$ acceptor state can be determined as well, resulting in a value of $\sigma_p = 2.15 \times 10^{-13} \text{ cm}^2$.

It is worth mentioning here that the ~30% decrease of the leakage current due to the transformation of V_3 from PHR to FFC configuration in the DOFZ diode (doping $8 \times 10^{11} \text{ cm}^{-3}$) irradiated with 6 MeV electrons and $\Phi = 1.55 \times 10^{12} \text{ cm}^{-2}$, depicted in Fig. 4(b), is not common to all the investigated cases. Thus, for the same electrons energy, by increasing the irradiation fluence, although the introduction rate of V_3 in the PHR configuration remains the same, the decrease of the leakage current during the annealing out V_3 in PHR configuration is less and less pronounced becoming of ~10% for diodes irradiated with 6 MeV electrons and $\Phi = 5.9 \times 10^{13} \text{ cm}^{-2}$. On the other hand, by increasing the electron energy to 15 MeV or 27 MeV, the introduction rate of V_3 in PHR configuration increases roughly with a factor of 3 and its contribution to the leakage current increases. For example, the decrease of the leakage current measured in samples irradiated with 27 MeV electrons is about 60% for $\Phi = 7.5 \times 10^{12} \text{ cm}^{-2}$ (V_3 in PHR configuration monitored by DLTS) and below 10% for heavily irradiated samples (measured by TSC where V_3 could not be monitored—measurements described later on). In the latter

case, several other defects start to be generated (as I_p —second order point defect and other complex defects) and they may have important contributions to the leakage current. Thus, while the contribution of V_3 to the leakage current increases with electron energy it decreases with increasing the irradiation fluence.

Other point and extended defects can be observed after irradiation with larger fluence values, using the TSC technique, where the DLTS method is not applicable anymore. Examples of TSC spectra obtained after irradiation with electrons of different energies and for a fluence of $\Phi = 2.2 \times 10^{14} \text{ cm}^{-2}$ are given in Fig. 5(a). The filling of the traps was done at 10 K by injecting a forward current of 2 mA for 30 s. It is worth mentioning that, similar to the DLTS technique, by forward injection not all the electrically active defects can be filled and thus, detected in the corresponding TSC spectrum. The density of electrons (n_t) or holes (p_t) trapped at the filling temperature (T_{fill}) on a certain defect depends on the values of σ_n and σ_p according to^{26,40–42}

$$n_t(T_{fill}) = N_t \frac{\sigma_n(T_{fill}) \times v_{th,n}(T_{fill})}{\sigma_n(T_{fill}) \times v_{th,n}(T_{fill}) + \sigma_p(T_{fill}) \times v_{th,p}(T_{fill})};$$

$$p_t(T_{fill}) = N_t - n_t(T_{fill}). \quad (4)$$

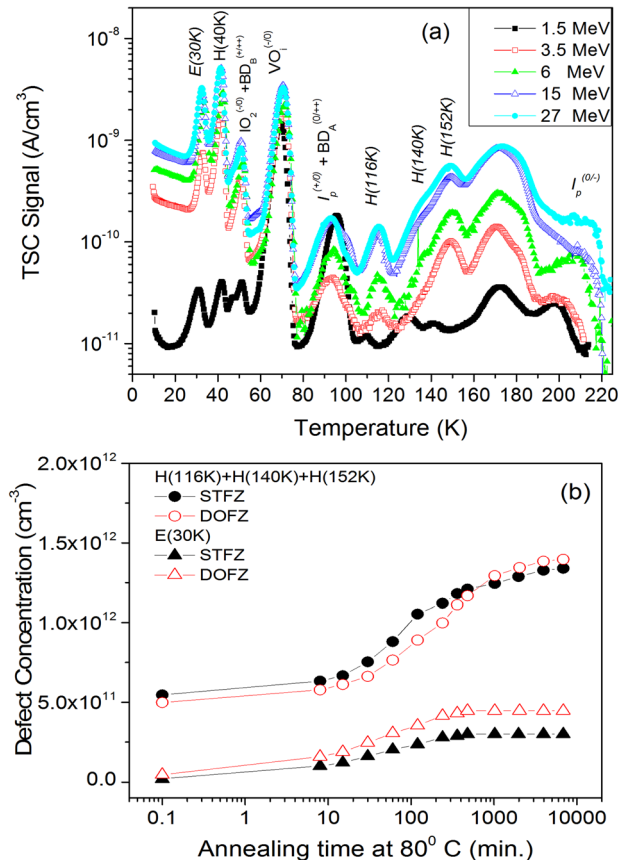


FIG. 5. (a) TSC spectra after irradiation with different electron energies and normalized to $\Phi = 2.2 \times 10^{14} \text{ cm}^{-2}$, measured on DOFZ material after annealing for 8 min at 80 °C; (b) annealing-in of $H(116 \text{ K})$, $H(140 \text{ K})$, and $H(152 \text{ K})$ defects in STFZ and DOFZ diodes irradiated with 15 MeV electrons and $\Phi = 2.2 \times 10^{14} \text{ cm}^{-2}$ —annealing performed at 80 °C. Filling of the traps was performed at 10 K by 2 mA forward injection for 30 s.

Thus, after forward injection electron traps having $\sigma_p \gg \sigma_n$ (e.g., $V_2^{-1/0}$ (Ref. 18) and $V_3^{-1/0}$ (Ref. 30 and this work)) or hole traps with $\sigma_n \gg \sigma_p$ (e.g., $C_iO_i^{+1/0}$ at low temperatures^{18,29}) cannot be filled to give rise to a TSC emission peak.

Known as point defects in Fig. 5(a) (detected also after gamma-irradiation) are: IO_2 (the interstitial oxygen dimer), VO_i , the BD, and the I_p defects.^{10,23,26} Several other defects, among which H(116 K), H140 K), and H(152 K) are acceptors in the lower part of the silicon bandgap and E(30 K) is a shallow donor in the upper part of the gap, are also known from hadron irradiations¹⁰ but not seen after irradiations with ^{60}Co - γ -rays,^{8,10,23,24} as expected because of the low electron energy. As can be observed in Fig. 5(a), these electrically active defects can already be detected in very small concentrations after irradiation with high fluence of 1.5 MeV electrons, and their generation increases with the electron energy suggesting that they are extended defects. It is worth mentioning that the E(30 K) defect is not detected immediately after irradiation.²⁹ This defect anneals-in after irradiation is stopped reaching its maximum concentration after ~ 200 min annealing at $80^\circ C$. The TSC signals from H(116 K), H140 K), and H(152 K) defects continue to grow during much longer times after the irradiation is performed and tend to stabilize after 4000 min—see Fig. 5(b). Due to the strong overlapping of the TSC signals from H(140 K) and H(152 K) defects, an estimation of their generation rates can be properly done only by considering them together. The fluence dependence can be estimated from the saturated values (after annealing of 4000 min at $80^\circ C$) of the defect concentrations (determined by integrating the corresponding TSC peaks), obtained on samples exposed to different irradiation levels. A good example in this respect is given in Fig. 6(a) for 6 STFZ samples irradiated with 6 MeV electrons in a fluence range between 2×10^{14} and $1.2 \times 10^{15} \text{ cm}^{-2}$. As it can be observed, all the E(30 K) and the H defects are generated in concentrations increasing linearly with the irradiation fluences. For these centers, the fit in the log-log scale it is done by fixing the slope to 1. The same figure shows also the concentration of the I_p point defect versus fluence, fitted by fixing the slope to 2, as the only example of a defect with a non-linear fluence dependence (in fact quadratic) found so far. Thus, for E(30 K) and the H defects, the results are given in Fig. 6(b). A saturation of the rates for all these cluster-related defects starts to be observed around 15 MeV electron energy. One can observe that only the generation of E(30 K) defect is influenced by the oxygen content. This is clearly seen for electron energies larger than 3.5 MeV where the introduction rate is significantly larger ($\sim 40\%$) in DOFZ compared to STFZ. In contrast, although a slight difference in the annealing-in time dependence exists between STFZ and DOFZ materials (see Fig. 5(b)), the generation rates for the H defects are very similar indicating that oxygen is not directly involved in the formation of these defects, leading to the supposition that they might be related to higher order vacancy complexes ($V_{n>3}$).

Relevant for applications is whether the radiation induced defects affect the sensor characteristics at their operational temperature and to what extent. As acceptors in the lower part of the gap, the H defects have a direct impact

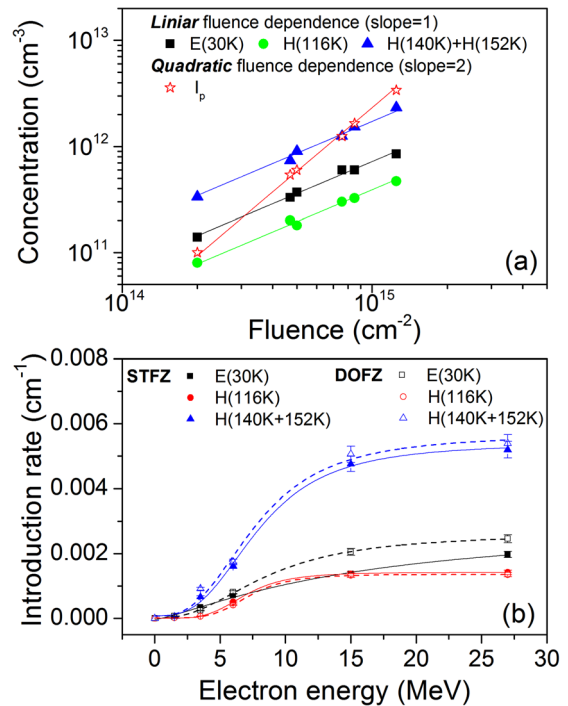


FIG. 6. (a) Fluence dependence: defect concentrations (symbols) in STFZ samples irradiated with different fluences of 6 MeV electrons. The lines represent the linear fits performed with fixing the slope = 1 for E(30 K), H(116 K) and H(140 K) + H(152 K) and slope = 2 for the I_p defects. The correlation coefficients for these fits are all above 0.99. (b) Introduction rates of extended defects E(30 K), H(116 K), H(140 K), and H(152 K) in STFZ and DOFZ materials as function of electron energy.

(contributing with negative charge) on the effective space charge concentration of the irradiated diodes. Similar, the E(30 K) donor, with an energy level close to E_C contributes also in full concentration with positive charge to N_{eff} at ambient temperatures. Accounting also for the negative charge introduced by the I_p defect via its single acceptor level $I_p^{0/-}$, giving rise to a TSC peak around 200 K, and for the BD donor, the N_{eff} can be calculated according to Eqs. (2) and (3). The resulting N_{eff} calculated on the basis of the defect concentrations determined from TSC experiments for a temperature of $20^\circ C$ is given in Fig. 7 for the STFZ and DOFZ diodes irradiated with 15 MeV electrons. In the same figure, the N_{eff} determined from the experimental C-V curves is given as well. One can observe that both types of diodes undergo space charge sign inversion (get “inverted”) during the annealing time, resulting in negative values of N_{eff} at the end of the annealing. As already known, the higher oxygen content in DOFZ compared with STFZ material favors the formation of shallow donors (as BD and E(30 K)), while the generation of the close to midgap acceptor like defect I_p is suppressed. This, together with the faster annealing-in of the H defects in STFZ compared with DOFZ material (see Fig. 5(b)) leads to a delay in the appearance of the “type inversion” effect in DOFZ diodes. The good agreement between the two methods of determining the N_{eff} in irradiated diodes confirms that the defects determining the changes of the device performance at ambient temperatures after irradiation is stopped are not the point defects but the small clusters of defects as E(30 K), H(116 K), H(140 K), and H(152 K).

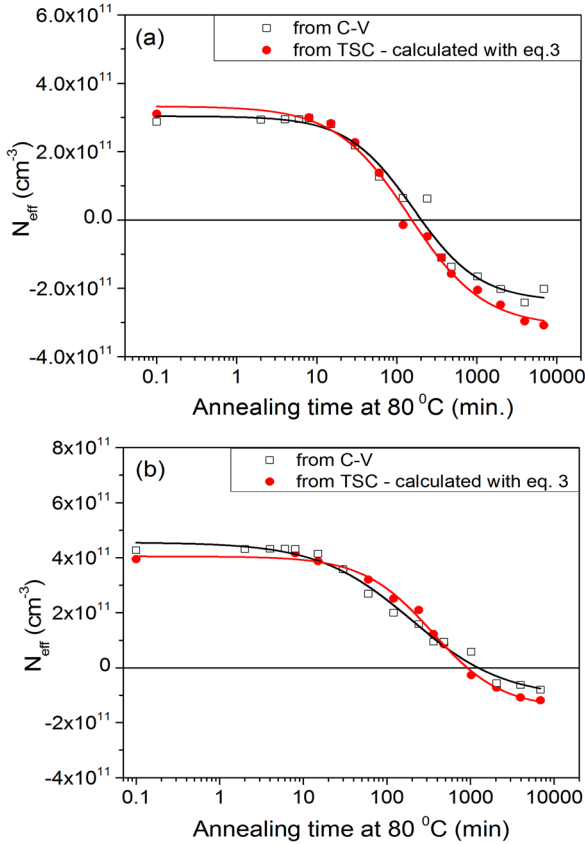


FIG. 7. The effective doping concentration, as determined from C-V characteristics at 20 °C (open symbols) or calculated with Eq. (3) and accounting the defect concentration evaluated from TSC experiments, versus annealing time at 80 °C, after irradiation with 15 MeV electrons, of: (a) STFZ diode $\Phi = 2.18 \times 10^{14} \text{ cm}^{-2}$; (b) DOFZ diode, $\Phi = 1.96 \times 10^{14} \text{ cm}^{-2}$.

In addition, there are indications that part of the H defects can change their configuration at RT from an electrically active one giving rise to H(116 K) and H(140 K + 152 K) TSC peaks to an electrically inactive one (without energy levels in the bandgap of silicon) undetectable in electrical measurements. This phenomenon is observed in inverted diodes. An example is given in Fig. 8 for a STFZ diode irradiated with 27 MeV electrons, $\Phi = 3.56 \times 10^{14} \text{ cm}^{-2}$ and annealed for 3960 min at 80 °C. It can be observed that after the heat treatment at 80 °C the magnitudes of the H(116 K) and H(140 K + 152 K) peaks decrease if the diode is kept few hours in the dark at RT (compare curves 1 and 2 in Fig. 8(a)). The difference in the H(116 K) and H(140 K + 152 K) defect concentration is $\Delta[H]_{1-2} = 2.4 \times 10^{11} \text{ cm}^{-3}$. This change in the defect concentration, reflected fully as a decrease of N_{eff} in “type” inverted diodes, should lower the depletion voltage V_{dep} by 14.3 V ($V_{\text{dep}} = qd^2N_{\text{eff}}/2\varepsilon_0\varepsilon_r$, with ε_0 and ε_r being the vacuum permittivity and the relative dielectric constant of silicon, respectively). Indeed, a decrease of V_{dep} with ~ 15 V is seen in the C-V characteristics (compare curves 1 and 2 in Fig. 8(b)). As shown in Fig. 8(c), no change in the saturation value of the leakage current (for $V > V_{\text{dep}}$) is observed. The I-V shape is typical for diodes after “type inversion.” Depletion starts at the rear (n^+) side which has an about 4 times larger area compared to the p^+ electrode, and with increasing reverse bias the depleted volume is much larger compared to the one when the

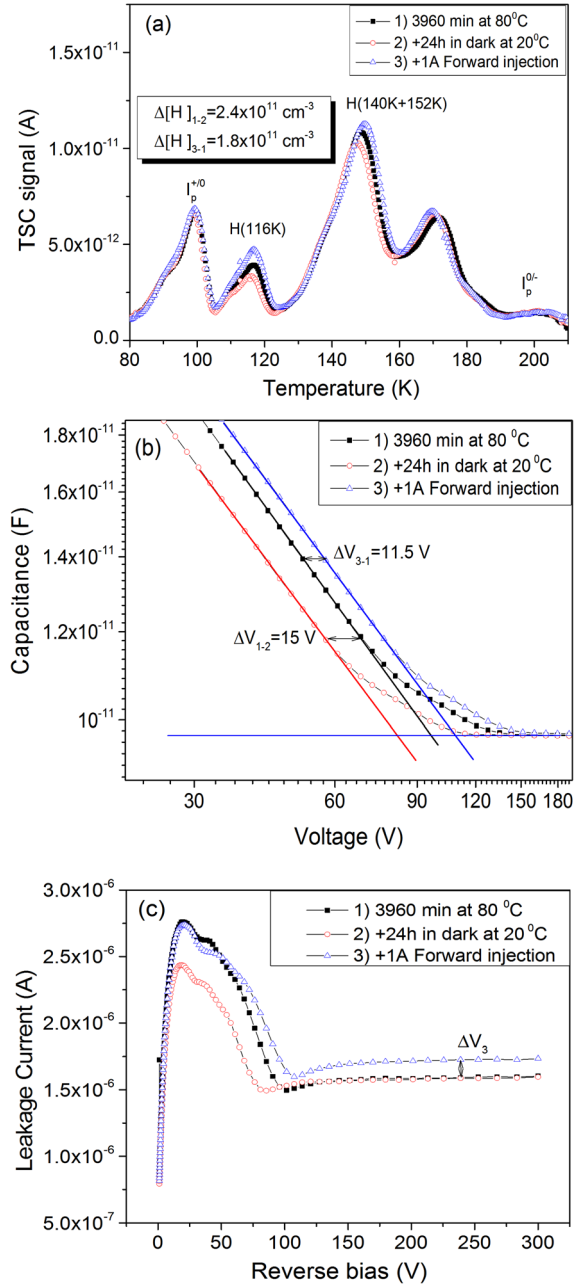


FIG. 8. Bistability of H(116 K), H(140 K), and H(152 K) defects and corresponding change in the depletion voltage of a STFZ diode irradiated with 27 MeV electrons, $\Phi = 3.56 \times 10^{14} \text{ cm}^{-2}$ and annealed for 3960 min at 80 °C: (a) TSC spectra; (b) C-V curves measured with a frequency of 10 kHz and 0.5 V small ac signal; and (c) I-V characteristics measured all at 20 °C. The measurements were performed consecutively, the first just after the annealing (curves 1), the second 24 h after annealing while the sample was kept in dark at 290 K (curves 2), and the third ones after performing a 1 A forward injection at 0 °C (curves 3) for 30 min.

depletion starts from the p^+ contact (for non-inverted diodes). When full depletion is achieved the guard ring start to act as a current collection ring for the outer part of the current distribution, which results in a sudden decrease of the p^+ pad current to a value which corresponds to the volume given by the p^+ area and the thickness of the device.

It can be observed that by forward injection (1 A, 30 min at RT) one not only regains the original TSC peaks measured immediately after the annealing at 80 °C but also even larger

TSC signals are measured (curve 3 in Fig. 8(a)). The increase in concentration is $\Delta[H]_{3-1} = 1.8 \times 10^{11} \text{ cm}^{-3}$ compared with the first measurements (compare curves 1 and 3 in Fig. 8(a)). Accordingly, the depletion voltage should increase with 10.7 V, close to 11.5 V value determined from C-V characteristics (compare curves 1 and 3 in Fig. 8(b)). In addition, the 1 A forward injection causes an increase of the leakage current by $\sim 0.15 \mu\text{A}$ (compare curves 1, 2, and 3 in Fig. 8(c)) that cannot be connected with the variation of the H defects concentration. As discussed previously, the 1 A forward injection can change the configuration of V_3 defects, from FFC (common after long time annealing) to PHR (seen some time after irradiation or activated after 1 A forward injection).^{28,30,31} Therefore, we interpret this $\sim 8\%$ change in the leakage current as an increase of the concentration of V_3 in PHR configuration with respect to the FFC one. Due to the similar bistability of the V_3 and H defects, it is tempting to associate the H(116 K) and H(140 K + H152 K) defects with higher order of vacancy clusters as tetra- and penta-vacancies, in agreement with *ab initio* calculations presented in Ref. 46 predicting that in silicon V_3 , V_4 , and V_5 have two configurations, one of PHR type and a more stable but electrically inactive FFC one. However, for V_3 in the FFC configuration, a shallow donor labeled E_{75} was found.³⁰

B. Investigation by HRTEM

STFZ and DOFZ silicon wafers irradiated with 15 MeV electrons at a fluence of $1 \times 10^{16} \text{ cm}^{-2}$ and 27 MeV electrons at a fluence of $2 \times 10^{16} \text{ cm}^{-2}$, respectively, have been extensively studied by high resolution transmission electron microscopy.

Fig. 9(a) shows an HRTEM image along the [110] zone axis of the 15 MeV electron irradiated STFZ Si sample (as irradiated) revealing by the dark contrast the presence of clusters of point defects. Few are single cluster, i.e., a single darker dot, but most of them are agglomerated, either along the principal crystallographic directions forming darker lines of clusters, or randomly, giving rise to darker patches having dimensions of 3–5 nm. The density of defect clusters is very high. They are rather uniformly distributed in the lattice; therefore there is almost no region in the Si lattice not affected by their presence. It is worth mentioning that these types of defect clusters produced by high energy (15 MeV) electrons in Si and observed by HRTEM are not mentioned in literature. In earlier papers,^{47–51} the irradiation effects of much lower energy electrons (400 keV–1.5 MeV) have been studied by HRTEM. Since in our case a standard FZ Si wafer has been irradiated, the defect clusters can be formed by accumulation of in excess Si vacancies and self-interstitials, the end products of the collision cascade. Furthermore, because interstitials are very mobile at room temperature, it is likely to presume that the cluster of defects (single dark dots) consists mainly of vacancies, at least when they are not agglomerated along the principal crystallographic directions or in the black patches. It is known that a study at atomic scale of small defect clusters is not straightforward. Correct information can be obtained for the one dimensional (1D) or the two dimensional (2D) clusters which have a periodic

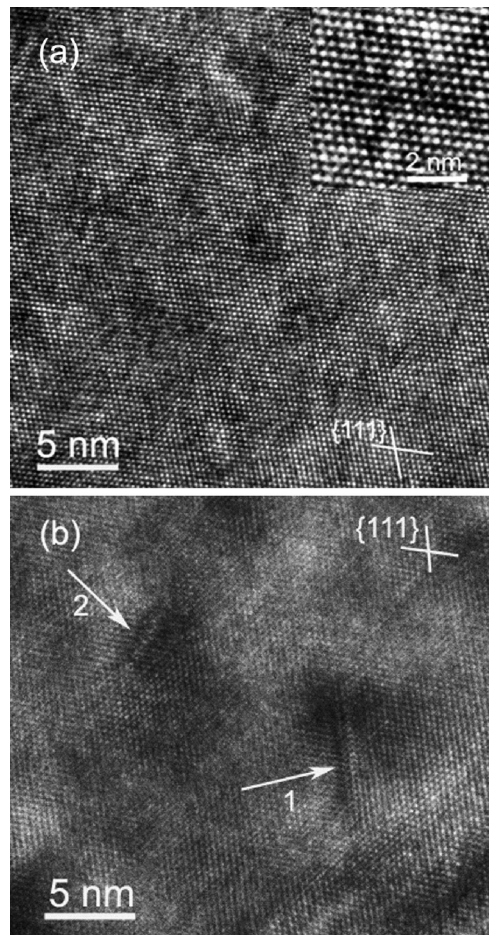


FIG. 9. HRTEM image along the [110] zone axis of the STFZ Si sample irradiated with 15 MeV electrons: (a) as irradiated, showing clusters of point defects revealed by the dotted dark contrast some agglomerated in dark patches or along the principal crystallographic directions are visible; inset detail of a star-like agglomerate of defect clusters; (b) annealed for 73380 min at 80 °C showing the appearance of two types of extended defects indicated by arrows: 1 the {111} defect and 2 the {113} defect.

structure along the electron beam, meaning the $\langle 110 \rangle$ direction, as in our case. The HRTEM images presented here were recorded close to Scherzer defocus, where the columns of atoms are seen in dark contrast, while the bright dots correspond to channels in the Si structure. Therefore, in the HRTEM images, the clustering of point defects is revealed by a dark contrast. A better understanding of the structure of these defect clusters need simulations of the HRTEM images on suitable models created with dedicated programs, which for the moment are not available in our laboratory.

Annealing at a low temperature for a long period of time reveals other types of extended defects. Fig. 9(b) shows that a long term annealing (73 380 min) at low temperatures (80 °C) determines the formation of extended defects such as the defect marked by arrow 1, detected by the distortions of the {111} planes, or the defect marked by arrow 2 located in the {113} habit planes. The dimensions of these extended defects are in the range of 3–6 nm. The {111} defect is an intrinsic Frank partial dislocation loop formed by the aggregation of vacancies in the (100) planes of Si. The formation of such defects was observed^{49,51} in FZ-Si samples irradiated *in-situ* with 400 keV and 1 MeV electrons, respectively. The

$\{113\}$ defects in Si irradiated with electrons were studied by HRTEM, in Refs. 47 and 51. As it has been pointed out, the $\{113\}$ defects result from the agglomeration of self-interstitials produced by a prolonged irradiation with 1 MeV electrons. It has been also suggested that self-interstitials are firstly arranged along the $\langle 110 \rangle$ directions and then nucleate in the $\{113\}$ planes.

The HRTEM results on the DOFZ Si sample irradiated with 27 MeV electrons at a fluence of $2 \times 10^{16} \text{ cm}^{-2}$ and further annealed at low temperatures are presented in the following.

As Fig. 10(a) reveals, the clusters of defects in the DOFZ Si wafer irradiated with 27 MeV electrons show a similar contrast as in the STFZ Si sample irradiated with 15 MeV electrons (see Fig. 9). As previously mentioned, they are distributed in the whole specimen at a comparable high concentration, meaning that the density of the introduced defect clusters, as observed in the HRTEM images, does not apparently differ, although the two samples were irradiated at different electron energies and fluences. It might appear an effect of saturation in the rate of introducing the clusters of defects at high energies, as indicated in Fig. 6(b) for the E(30 K), H(116 K), H(140 K), and H(152 K) smaller

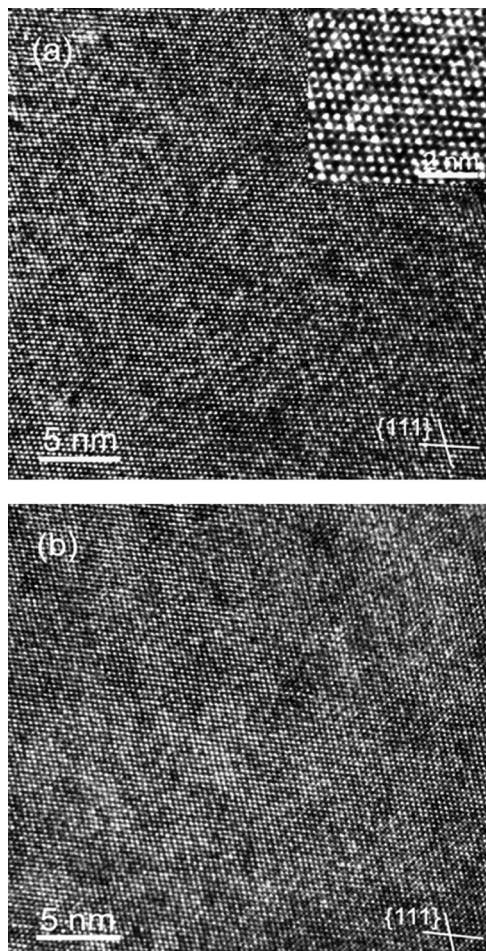


FIG. 10. HRTEM images along the $[110]$ zone axis of the DOFZ Si sample irradiated with 27 MeV electrons: (a) as irradiated, showing clusters of point defects, many grouped along the principal crystallographic directions; inset detail of an agglomerate of defect cluster; (b) annealed for 6860 min at 80°C.

clusters of point defects. On the other hand, regardless of the presence of diffused oxygen in the Si samples (STFZ vs. DOFZ), the clusters of point defects show similar contrast. It looks like that the clusters of defects observed by HRTEM are not related to the presence of oxygen in the samples.

The effects of low temperature annealing are not easily observed by HRTEM. As Fig. 10(b) shows the low temperature annealing at 80°C produces an apparent migration of the clusters of point defects in the sense of de-grouping, especially those agglomerated along the principal crystallographic directions, and re-grouping and/or recombination. The result seems to be the appearance of zones where the Si lattice looks recovered (regions with brighter contrast) alternating with zones with agglomerates of defect clusters (black patches).

IV. MODELING OF DEFECT GENERATION

The most important process for radiation damage in silicon is the displacement of lattice atoms. The conventionally used value for the minimum threshold displacement energy (E_d) is 21 eV.⁵² Depending on the individual collision, the PKA energy can be much larger, thus producing a cascade of secondary recoils across its path. At the end of a recoil range, the non-ionizing interactions prevail, and dense agglomerates (*clusters*) of defects are formed. The threshold PKA energy for the production of clusters was calculated in the past to be about 5 keV.⁵³ Typically, *clusters* are large agglomerations of vacancies or interstitials in a volume of $\sim 20 \text{ nm}^3$ with 10^5 – 10^6 atoms.⁵⁴

A. Mott scattering

The primary interaction of energetic electrons with the silicon lattice atoms is governed by the Mott scattering. The general expression for Mott scattering is written as

$$\left(\frac{d\sigma}{d\Omega}\right)_{Mott} = \left(\frac{d\sigma}{d\Omega}\right)_{Rutherford} \times R_{Mott}. \quad (5)$$

Here, $(d\sigma/d\Omega)_{Rutherford}$ is the relativistic equation for Rutherford scattering and R_{Mott} the correction according to Mott. While the original Mott formula is quite complicated, the best practical approximation of it was given by Lijian *et al.*⁵⁵ These results are accurate within 1% for all atoms and electron energies between 30 keV and 900 MeV.

The relation between the kinetic silicon recoil energy E and the scattering angle ϑ is derived from relativistic kinematics as

$$E = \left(\frac{E_e^2 \beta^2}{M_{Si} c^2}\right) \times (1 - \cos \vartheta), \quad (6)$$

and for the recoil energy distribution we get

$$\left(\frac{d\sigma}{dE}\right) = \left(\frac{E_e^2 \beta^2}{M_{Si} c^2}\right) \times \left(\frac{d\sigma}{d(\cos \vartheta)}\right), \quad (7)$$

which using $d\Omega = 2\pi d(\cos \vartheta)$ can then be derived from Eqs. (5) and (6) together with the results from Lijian for R_{Mott} .

According to Eq. (7), $d\sigma/dE$ is displayed in Fig. 11(a). It should be noted, however, that for simplicity the screening effect of the atomic shell had been disregarded.

B. Damage functions

The formation of point defects or clusters largely depends on the local density of generated displacements. For $E_e = 1.5 \text{ MeV}$ (with a maximum recoil energy of 300 eV) a maximum of 14 displacements is calculated. Including likely recombination effects for closed Frenkel pairs, one would not expect more than a few surviving displacements, certainly not enough to be responsible for clustering formation. The maximum recoil energy increases with the increasing electron energy, therefore this would lead to a stronger increase of the cluster-related defects compared to that of point-like defects. This is verified by the present results (see Sec. IV C below).

There are two different approaches for describing the Non Ionizing Energy Loss (NIEL) which is responsible for displacement damage:

– Classical NIEL: The classical description is based on two body elastic collisions between the PKA's and any further secondary recoils in the collision cascade with the lattice atoms (binary calculations). It deals with the lattice as being at zero absolute temperature neglecting the

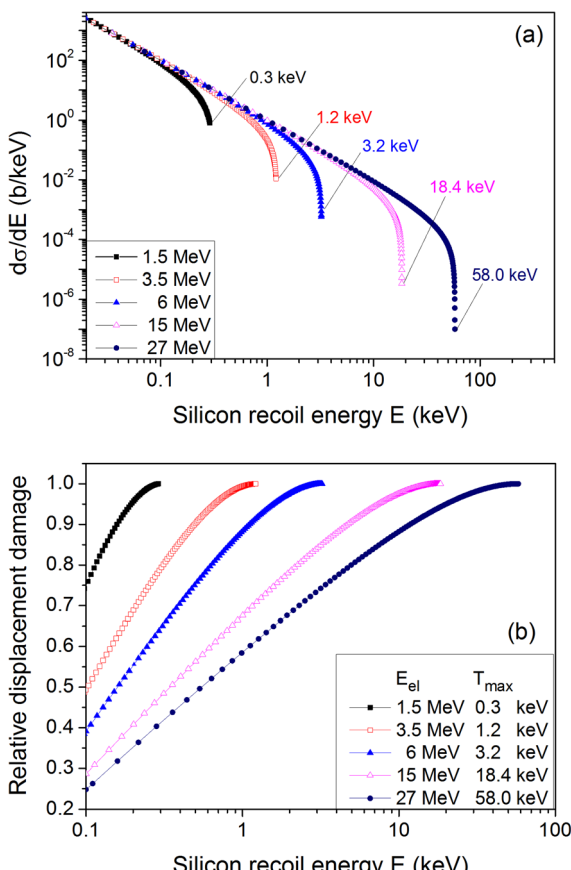


FIG. 11. (a) Differential Mott cross section for different electron energies according to Eq. (7). (b) Relative displacement damage as function of recoil energy E .

enormous localized heating due to the energy dissipation in the dense regions of the collision cascade.

– Effective NIEL: Using molecular dynamics (MD) simulations, many body interactions are taken into account. At low recoil energies, the results are predominantly different from the classical approach. Even below the displacement threshold, the combined interaction with many atoms may lead to displacements.⁵²

While the classical NIEL might still be applicable for the cascade region with sparsely distributed Frenkel pairs, presumably responsible for isolated point defects, we assume that the formation of cluster related defects, related to collisions with a high localized density of energy dissipation, as present at the end of the collision cascade, is better described by using MD simulations.

1. Classical NIEL

The basic equation for NIEL as function of the electron energy E_e is given by

$$\text{NIEL}(E_e) = \frac{N_A}{A} \int_{E_{\min}}^{E_{\max}} Q(E) E \left(\frac{d\sigma}{dE} \right) dE, \quad (8)$$

where the integral is over all recoil energies E with $E_{\min} = E_d = 0.21 \text{ eV}$ and E_{\max} given by the relativistic equation

$$E_{\max} = \frac{2E_e(E_e + 2m_e c^2)}{M_0 c^2 A_{Si}}. \quad (9)$$

N_A = Avogadro number, A = mass of the silicon atom in amu, E the kinetic energy of the PKA, and $d\sigma/dE$ the differential cross section for the Mott scattering as described above. Q is the Lindhard partition function,⁵⁶ which describes that part of the recoil energy responsible for displacements

$$Q = \frac{1}{1 + k_L g(\varepsilon)}. \quad (10)$$

In our case: $k_L = 0.146$ and $\varepsilon = E/41.05$ with E in keV. The most recent evaluation for $g(\varepsilon)$ is given by Akkerman *et al.*⁵⁷ and used here

$$g = 0.74422\varepsilon + 1.6812\varepsilon^{3/4} + 3.4008\varepsilon^{1/6}. \quad (11)$$

Using the input given by Eqs. (10) and (11), the displacement damage for a recoil energy E can then be written as $E \cdot Q \cdot d\sigma/dE$. Using the full integral for normalization, the relative displacement damage is plotted in Fig. 11(b). It is obvious that for larger electron energies, the damage part increases significantly and thus most likely the ratio of cluster to point defects. The best compilation of the classical NIEL for electrons is given by Jun *et al.*⁵⁸ They have used the Lijian parameterization for the Mott scattering, taking also the screening effect of the atomic shell into account (Fig. 12(a)).

As an alternative to the analytical approach one may also use binary code simulations. SRIM/TRIM is the most

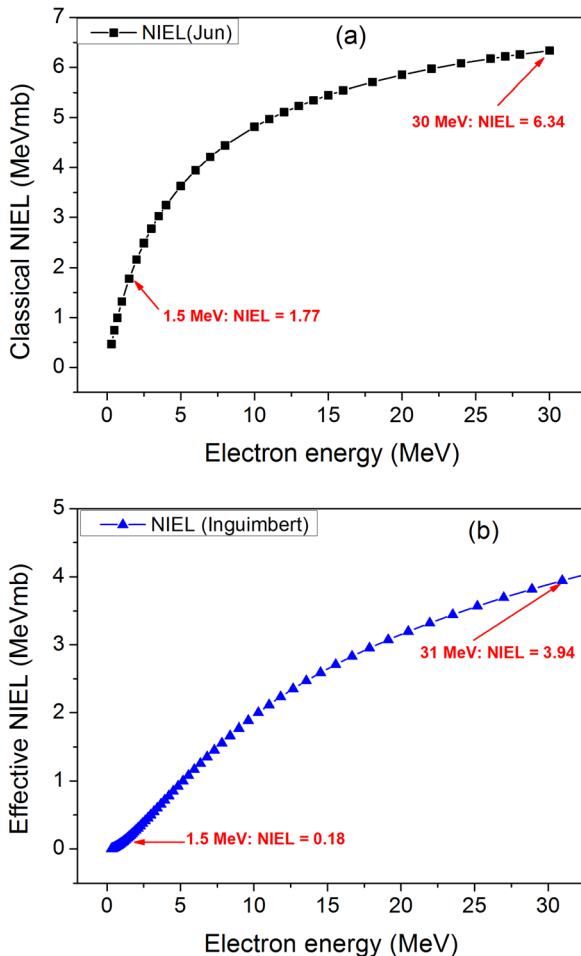


FIG. 12. (a) Classical NIEL as function of electron energy. (b) Effective NIEL as function of electron energy.

widely used program which can—in addition to various other applications—easily be used for computing the number of vacancies (and hence Frenkel pairs) for any recoil energy.⁵⁹ Trim is very simple to use, gives direct results and

statistics can be achieved easily by starting the program with different “random numbers.” However, the silicon is regarded to be amorphous and as also in other binary code simulations taken at zero absolute temperature. Crystal TRIM (or TCAS) is another binary code which delivers—specialized to silicon—very useful results.⁶⁰ We used a slightly modified version provided by Posselt.⁶¹ Contrary to TRIM, TCAS uses the crystalline structure of silicon. Channeling effects are avoided by using appropriate incident angles, 3-dimensional representation of the vacancy and interstitial distribution is available and in a second step intra-cascade V-I recombination is included. The results are useful for further random walk simulations. As an example, the initial collision cascade for a 20 keV PKA is shown in Fig. 13(a), and the result after intra-cascade recombination of close Frenkel pairs is shown in Fig. 13(b). Only about 20% of the initially generated vacancies and interstitials are surviving. It is worth noting that in the example of Fig. 13, there is a dense agglomeration of interstitials and vacancies in the area $\Delta x \times \Delta y \times \Delta z \approx 20 \text{ nm}^3$, hence likely giving rise to the defect clusters observed in HRTEM experiments (see Figs. 9 and 10). In other branches of the cascade, one observes more isolated displacements.

An analytical expression for calculating the number of Frenkel pairs was proposed by Kinchin and Pease,⁶² and later on modified by Norgett *et al.*,⁶³ where the originally used PKA-energy (as in Ref. 62) is replaced by the energy responsible for displacements as given by the partition function from Eq. (10). TRIM, respectively, TCAS results are, after proper normalization, almost identical and lead to very similar results as from Eq. (10). For comparison with experimental results, the damage function of Jun *et al.*⁵⁸ is used.

2. Effective NIEL

Contrary to the binary code approach used for the classical NIEL results from MD models had been applied for a different calculation of NIEL. A very nice discussion of this

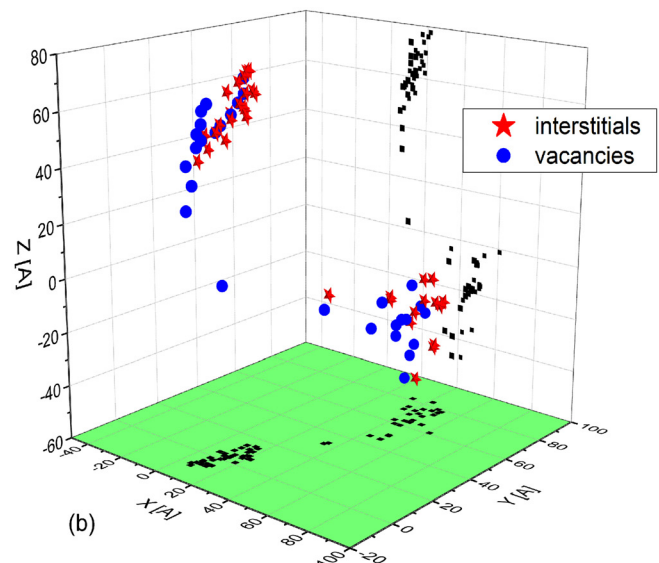
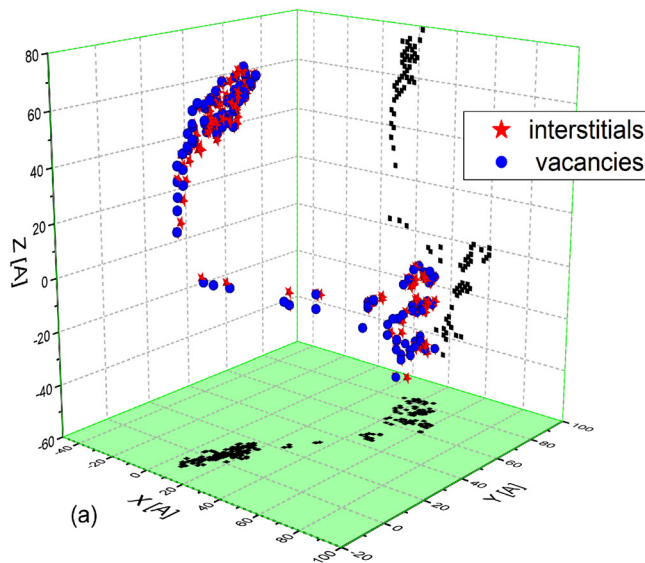


FIG. 13. Example of a collision cascade generated by a 20 keV PKA as simulated by TCAS. 2 cascade branches are visible. (a) Original cascade; (b) after V-I recombination, all scales in Å.

effective NIEL is given by Inguimbert *et al.*,⁵² where most relevant literature is cited. In contrast to classical NIEL calculations, collective atomic motion is taken into account, the enormous energy dissipation leads to melting in localized small areas with re-crystallization of these initially amorphous pockets at later stages. This transition from initially formed amorphous pockets to recrystallization at later phases is nicely documented in the MD calculations performed by Caturla *et al.*⁶⁴ It is shown, that for a PKA energy of 5 keV and after relaxation during 8 ps there are still about 500 displacement atoms left, much more than would be calculated via binary code approximation (BCA). A comparison of measured experimental results with respect to the conventional and effective NIEL calculations was published by Arnalda *et al.*⁶⁵ It is shown that for electron irradiation the difference between classical NIEL and effective NIEL is much larger than for proton irradiation. This is expected since Mott scattering of electrons leads to a majority of recoils at low energies (see Fig. 11) for which MD calculations predict a much larger number of displaced atoms than predicted by BCA. Therefore, the effective NIEL approach should be very interesting in comparison with our electron irradiation results. As shown in Fig. 12 in the electron energy range between 1.5 and 30 MeV, the classical NIEL increases only by a factor of ~ 4 , whereas the effective NIEL rises much more rapidly by a factor of 20.

C. Comparison with experimental results

One of the most obvious radiation induced degradation effects in silicon particle detectors is the increase of the reverse current. The effect is described by the (current related) damage rate α , which is defined according to

$$\frac{I}{V} = \alpha \times \Phi, \quad (12)$$

in which I is the reverse current at full depletion, V is the active volume of the diode, and Φ is the particle fluence (number of incident particles per cm^2). In radiation damage studies with high energy charged hadrons (protons or pions), respectively, MeV neutrons, the damage rate α is proportional to the classical NIEL.⁶⁶ In the present study, α was measured for electron energies between 1.5 and 27 MeV and the results are shown in Fig. 14. Clearly, the damage rate is not proportional to the classical NIEL but instead shows an almost linear dependence on the effective NIEL (Fig. 14(b)). Hence for electron irradiation, the α -value seems to be correlated to cluster defects. In fact, the various attempts to explain the current as generated by point defects have been not very convincing. On the other hand, in an early report by McEvoy *et al.*,⁶⁷ it was suggested that the high local density of defects in the terminal clusters may lead to a direct charge exchange between closely spaced defects. This so called *inter-defect charge exchange* would, e.g., enhance the charge carrier generation rate by more than one order of magnitude, assuming a local density of $\sim 10^{19} \text{ cm}^{-3}$. More details of such calculations are given in an earlier report by Gill *et al.*⁶⁸

In Fig. 15, the introduction rates for VO and V_2 are displayed with respect to NIEL, both certainly point defects and

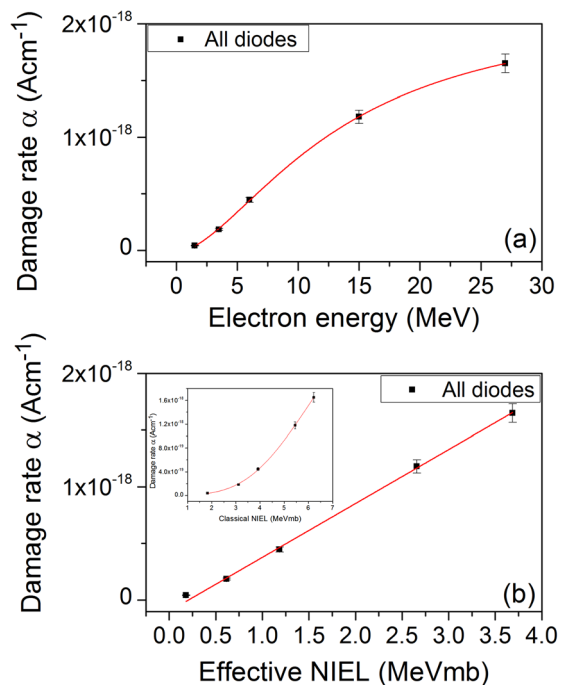


FIG. 14. Current related damage rate α : (a) as function of electron energy and (b) linear dependence on effective NIEL in contrast to classical NIEL (inset).

hence, as expected very well described by a linear dependence on the classical NIEL, the correlation with effective NIEL is nonlinear (see inset).

The deep acceptor-like defects (H116K, H140K, and H152K) as well as the donor E(30K) had been described in Sec. III as extended, cluster related, defects. This is very nicely in accordance with the results of Fig. 16. Here, it is shown that the introduction rates, calculated after 8 min

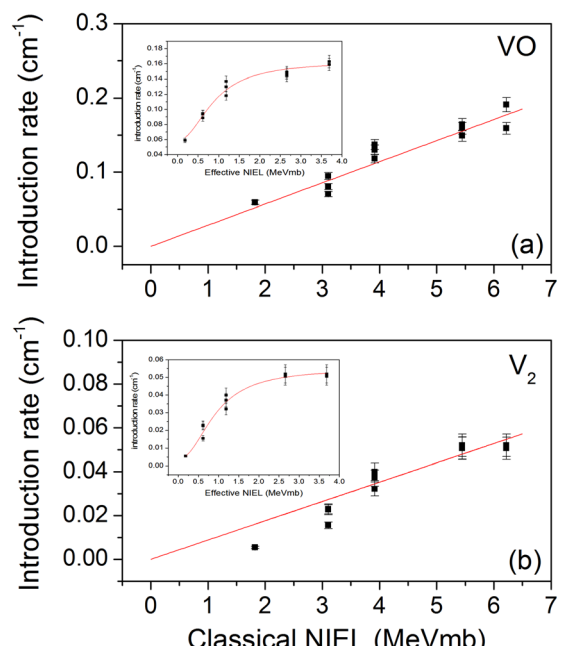


FIG. 15. Introduction rates for VO (a) and V_2 (b), correlation with classical and effective NIEL (inset). Introduction rates from DLTS, samples as irradiated.

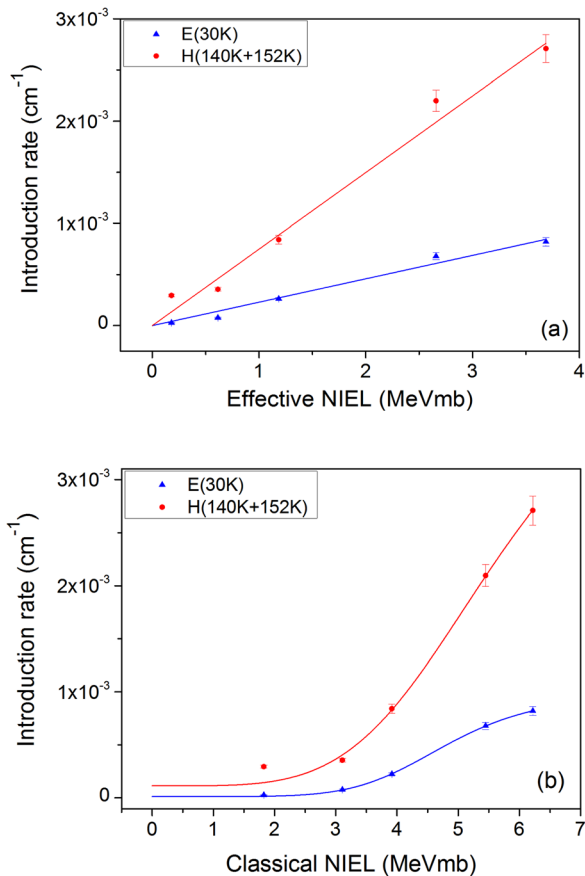


FIG. 16. Introduction rates of the E(30 K) and H(140 K + 152 K) in DOFZ silicon, TSC measurements after 8 min at 80 °C annealing. (a) Dependence on effective NIEL and (b) dependence on classical NIEL.

annealing at 80 °C, depend linearly on effective NIEL (Fig. 16(a)), in contrast to classical NIEL (Fig. 16(b)).

If we now consider the E(30 K) defect as being representative for the formation of extended (cluster) defects and VO as an isolated point defect, the ratio of both introduction rates as function of electron energy should be equivalent to the increase of cluster to point defects. In the electron energy range between 1.5 and 27 MeV, this ratio increases by roughly a factor of 10 (Fig. 17).

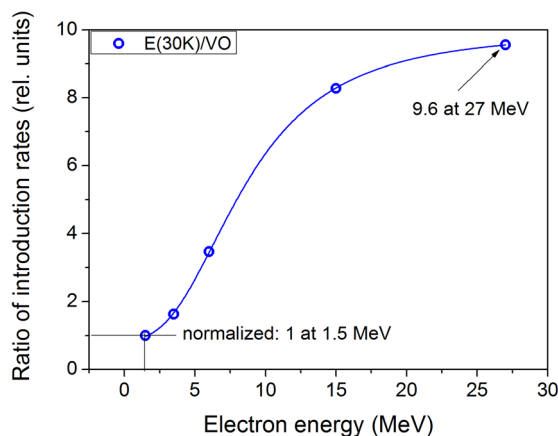


FIG. 17. Normalized ratio of introduction rates for E(30 K) (8 min/80 °C) and VO(as irradiated) for DOFZ silicon as function of electron energy.

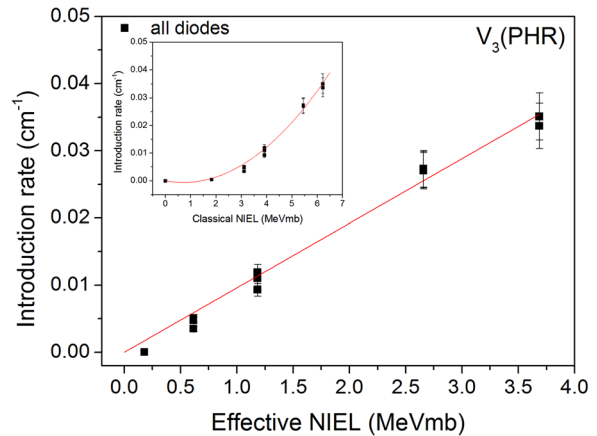


FIG. 18. Dependence of introduction rate for V₃ on effective NIEL and classical NIEL (inset); DLTS measurements, samples as irradiated.

It is interesting to study the dependence of the defect V₃ with respect to NIEL. Though the double-vacancy V₂ can be generated directly (assumed displacement energy 42 eV) as an isolated point defect, this is certainly not to be expected for the tri-vacancy, formed via V₂ + V → V₃, most likely in vacancy agglomerations, not necessarily dense clusters. In fact, Fig. 18 shows that the introduction rate is proportional to effective NIEL (as expected for cluster effects), while a linear correlation with classical NIEL can be ruled out (see inset). Most damage studies in silicon detectors for high energy elementary particle experiments had been performed using GeV-protons and MeV-neutrons.⁶⁹ This has the advantage of resembling the energy range of the relevant hadrons responsible for damage induced degradation of the detector performance. However, as related to their individual interaction with the silicon atoms, both point and cluster effects are responsible and the association of certain defects with either of them remained rather speculative. This unsatisfied situation had been improved appreciably by the present study, by which several defects can either be identified as isolated point or cluster related ones. At the same time, our results show that the conventionally used classical NIEL description should be used with great caution, probably not only for electron irradiation.

V. CONCLUSIONS

The study of n-type silicon diodes irradiated with electrons of energies ranging from 1.5 MeV to 27 MeV have enabled us to scan the generation of point defects and small clusters of defects. It is shown that after low irradiation fluence mainly point defects are generated, the largest electrically active defect detected being the tri-vacancy (V₃). This defect starts to be detected after irradiation with electrons of 3.5 MeV. Annealing experiments at 80 °C revealed that the V₃ defect and the leakage current show similar time constants, indicating that the variation seen in the leakage current is entirely related to the change in the concentration of V₃ in PHR configuration. From this correlation, the capture cross section for holes of the (V₃⁽⁻⁰⁾) was determined to be $\sigma_p = 2.15 \times 10^{-13} \text{ cm}^2$. Other small defect clusters (labeled as E(30 K), H(116 K), H(140 K), and H(152 K)) are detected

after high irradiation fluence values already for an electron energy of 1.5 MeV. The change of the space charge density with irradiation and with the annealing time after irradiation is fully described by accounting for the radiation induced trapping centers. The H(116 K), H(140 K), and H(152 K) defects are bistable, the change between the defect configurations being reversible at ambient temperatures. Only for one configuration, we detect energy levels in the bandgap of silicon. It is shown that the introduction rates of single vacancy (via the VO complex), di-vacancy, tri-vacancy, E(30 K), H(116 K), H(140 K), and H(152 K) defects increase with electron energy and saturate around 15 MeV. The generation of point defects as VO and V₂ it is well described with the classical NIEL approach accounting for two body elastic collisions between the PKA's and other secondary recoils in the collision cascade with the lattice atoms (binary calculations), while a linear dependence of introduction rates of the E(30 K) and H(140 K + 152 K) is obtained when molecular dynamics simulations with many body interactions are considered (effective NIEL). HRTEM investigations performed on samples irradiated with high energy electrons revealed the presence of clusters of point defects most of them agglomerated either along the principal crystallographic directions, or randomly, giving rise to dark patches with dimensions in the 3–6 nm range. The annealing at 80 °C produces an apparent migration of the defect clusters in the sense of de-grouping and re-grouping and/or recombination. The clusters of point defects generated by irradiation with electrons of 15 MeV and 27 MeV in oxygen-lean and oxygen-rich materials, respectively, show similar contrast and distribution along the principal crystallographic directions, indicating that the clusters of defects observed by HRTEM are not related to the presence of oxygen in the samples.

ACKNOWLEDGMENTS

This work has been performed in the framework of the CERN-RD50 collaboration (WODEAN Project) and it was partly financed by the Romanian Authority for Scientific Research through the Project PCE 72/5.10.2011. R. Radu would like to thank especially to Robert Klanner in the frame of MC-PAD Project and German Academic Exchange Service (DAAD) for providing a fellowship (No. A1278811), which was essential for carrying out the work presented in this article. I. Pintilie would like to thank Alexander von Humboldt Foundation for providing the DLTS system, necessary for performing the measurements. G. Lindstroem is most thankful to M. Posselt for providing a modified version of TCAS. Thanks are also due to the teams at the irradiation facilities at Sao Paulo, PTB Braunschweig, and ELBE at Dresden-Rossendorf and especially to Michael Matysek for his engagement in preparing the set ups for the irradiations.

¹F. Gianotti, M. L. Mangano, and T. Virdee, *Eur. Phys. J. C* **39**, 293 (2005).

²See www.xfel.eu for free electron laser experiments.

³E. Fretwurst on behalf of the RD50 collaboration, *Nucl. Instrum. Methods A* **552**, 7 (2005).

⁴G. Kramberger on behalf of the RD50 collaboration, *Nucl. Instrum. Methods A* **583**, 49 (2007).

- ⁵A. Dierlamm, *Nucl. Instrum. Methods A* **624**, 396 (2010).
- ⁶R. Eber on behalf of the RD50 collaboration, *J. Instrum.* **9**, C02024 (2014).
- ⁷Z. Li, W. Chen, V. Eremin, R. Gul, Y. H. Guo, J. Harkonen, P. Luukka, E. Tuovinen, and E. Verbitskaya, *Nucl. Instrum. Methods A* **612**(3), 539 (2010).
- ⁸E. Fretwurst, G. Lindstroem, J. Stahl, I. Pintilie, Z. Li, J. Kierstead, E. Verbitskaya, and R. Roeder, *Nucl. Instrum. Methods A* **514**(1–3), 1 (2003).
- ⁹G. Kramberger, V. Cindro, I. Dolenc, I. Mandić, M. Mikuž, and M. Zavrtanik, *Nucl. Instrum. Methods A* **612**(2), 288 (2010).
- ¹⁰I. Pintilie, G. Lindstroem, A. Junkes, and E. Fretwurst, *Nucl. Instrum. Methods A* **611**, 52 (2009).
- ¹¹G. D. Watkins and J. W. Corbett, *Phys. Rev.* **121**(4), 1001 (1961).
- ¹²G. D. Watkins and J. W. Corbett, *Phys. Rev.* **134**(5A), A1359 (1964).
- ¹³G. D. Watkins and J. W. Corbett, *Phys. Rev.* **138**(2A), A543 (1965).
- ¹⁴S. D. Brotherton and P. Bradley, *J. Appl. Phys.* **53**, 5720 (1982).
- ¹⁵L. C. Kimerling, in *Radiation Effects in Semiconductors 1976*, Conference Series No. 31, edited by N. B. Urli and J. W. Corbett (The Institute of Physics, Bristol, 1977), p. 221.
- ¹⁶O. O. Awadelkarim, H. Weman, B. G. Svensson, and J. L. Lindström, *J. Appl. Phys.* **60**, 1974 (1986).
- ¹⁷B. G. Svensson, B. Mohadjeri, A. Hallén, J. H. Svensson, and J. W. Corbett, *Phys. Rev. B* **43**(3), 2292 (1991).
- ¹⁸A. Hallén, N. Keskitalo, F. Masszi, and V. Nágl, *J. Appl. Phys.* **79**, 3906 (1996).
- ¹⁹M. Moll, H. Feick, E. Fretwurst, G. Lindstroem, and C. Schultze, *Nucl. Instrum. Methods A* **388**, 335 (1997).
- ²⁰J. Hermansson, L. I. Murin, T. Hallberg, V. P. Markevich, J. L. Lindström, M. Kleverman, and B. G. Svensson, *Phys. B: Condens. Matter* **302**–**303**, 188 (2001).
- ²¹E. V. Monakhov, B. S. Avset, A. Hallén, and B. G. Svensson, *Phys. Rev. B* **65**, 233207 (2002).
- ²²I. Pintilie, E. Fretwurst, G. Lindstroem, and J. Stahl, *Appl. Phys. Lett.* **81**, 165 (2002).
- ²³I. Pintilie, E. Fretwurst, G. Lindström, and J. Stahl, *Appl. Phys. Lett.* **82**, 2169 (2003).
- ²⁴I. Pintilie, E. Fretwurst, G. Lindström, and J. Stahl, *Nucl. Instrum. Methods A* **514**, 18 (2003).
- ²⁵G. Davies, *Phys. Rev. B* **73**, 165202 (2006).
- ²⁶I. Pintilie, M. Buda, E. Fretwurst, G. Lindstroem, and J. Stahl, *Nucl. Instrum. Methods A* **556**(1), 197 (2006).
- ²⁷E. Fretwurst, F. Hönniger, G. Kramberger, G. Lindström, I. Pintilie, and R. Roder, *Nucl. Instrum. Methods A* **583**, 58 (2007).
- ²⁸R. M. Fleming, C. H. Seager, D. V. Lang, E. Bielejec, and J. M. Campbell, *Appl. Phys. Lett.* **90**, 172105 (2007).
- ²⁹I. Pintilie, E. Fretwurst, and G. Lindström, *Appl. Phys. Lett.* **92**, 024101 (2008).
- ³⁰V. P. Markevich, A. R. Peaker, S. B. Lastovskii, L. I. Murin, J. Coutinho, V. J. B. Torres, P. R. Briddon, L. Dobaczewski, E. V. Monakhov, and B. G. Svensson, *Phys. Rev. B* **80**, 235207 (2009).
- ³¹A. Junkes, D. Eckstein, I. Pintilie, L. F. Makarenko, and E. Fretwurst, *Nucl. Instr. and Meth. A* **612**, 525 (2010).
- ³²J. Coutinho, V. P. Markevich, A. R. Peaker, B. Hamilton, S. B. Lastovskii, L. I. Murin, B. J. Svensson, M. J. Rayson, and P. R. Briddon, *Phys. Rev. B* **86**, 174101 (2012).
- ³³V. P. Markevich, A. R. Peaker, B. Hamilton, S. B. Lastovskii, and L. I. Murin, *J. Appl. Phys.* **115**, 012004 (2014).
- ³⁴R. Radu, E. Fretwurst, R. Klanner, G. Lindstroem, and I. Pintilie, *Nucl. Instrum. Methods A* **730**, 84 (2013).
- ³⁵See <https://www.ipen.br> for IPEN-CNEN/SP.
- ³⁶See <http://www.bsu.by> for BUS.
- ³⁷See <http://www.ptb.de> for PTB.
- ³⁸See <http://www.hzdr.de> for ELBE.
- ³⁹I. Pintilie, L. Pintilie, M. Moll, E. Fretwurst, and G. Lindstroem, *Appl. Phys. Lett.* **78**(4), 550 (2001).
- ⁴⁰W. Shockley and W. T. Read, Jr., *Phys. Rev.* **87**, 835 (1952).
- ⁴¹R. N. Hall, *Phys. Rev.* **87**, 387 (1952).
- ⁴²L. Forbes and C-T. Sah, *Solid-State Electron.* **14**(2), 182 (1971).
- ⁴³J. W. Corbett and G. D. Watkins, *Phys. Rev.* **138**(2A), A555 (1965).
- ⁴⁴S. Wood, N. J. Doyle, J. A. Spitznagel, W. J. Choyke, R. M. More, J. N. McGuire, and R. B. Irwin, *IEEE Trans. Nucl. Sci.* **28**, 4107 (1981).
- ⁴⁵M. Moll, Ph.D. thesis, University of Hamburg, DESY THESIS-1999-040, December 1999.
- ⁴⁶D. V. Makarov and L. J. Lewis, *Phys. Rev. Lett.* **92**, 255504 (2004).
- ⁴⁷S. Takeda and T. Kamino, *Phys. Rev. B* **51**, 2148 (1995).

- ⁴⁸L. Fedina, J. Van Landuyt, J. Vanhellemont, and A. L. Aseev, *Nucl. Instrum. Methods Phys. Res., B* **112**, 133 (1996).
- ⁴⁹L. Fedina, A. Gutakovskii, A. Aseev, J. Van Landuyt, and J. Vanhellemont, *Phys. Status Solidi A* **171**, 147 (1999).
- ⁵⁰L. Fedina, O. Lebedev, G. Van Tendeloo, J. Van Landuyt, O. Mironov, and E. Parker, *Phys. Rev. B* **61**, 10336 (2000).
- ⁵¹S. Takeda, *Microsc. Res. Tech.* **40**, 313 (1998).
- ⁵²C. Inguimbert, P. Arnolda, T. Nuns, and G. Rolland, *IEEE Trans. Nucl. Sci.* **57**(4), 1915 (2010).
- ⁵³V. A. J. Van Lint, *Mechanisms of Radiation Effects in Electronic Materials* (John Wiley & Sons, 1980).
- ⁵⁴B. Gossick, *J. Appl. Phys.* **30**(8), 1214 (1959).
- ⁵⁵T. Lijian, H. Quing, and L. Zhengming, *Radiat. Phys. Chem.* **45**, 235 (1995).
- ⁵⁶J. Lindhard, V. Nielsen, M. Scharff, and P. V. Thomsen, *Mat. Fys. Medd. Dan. Vid. Selsk.* **33**(10), 1 (1963).
- ⁵⁷A. Akkerman, J. Baraka, M. B. Chadwick, J. Levinson, M. Murat, and Y. Lifshitz, *Radiat. Phys. Chem.* **62**, 301 (2001).
- ⁵⁸I. Jun, W. Kim, and R. Evans, *IEEE Trans. Nucl. Sci.* **56**(6), 3229 (2009).
- ⁵⁹J. F. Ziegler, J. P. Biersack, and M. D. Ziegler, "SRIM, Stopping and Range of Ions in Matter," see www.srim.org.
- ⁶⁰M. Posselt, "Crystal TRIM (TCAS)," see www.hzdr.de/FWI/FWIT/FILES/Manual_Crystal-TRIM.pdf.
- ⁶¹M. Posselt, Institute of Ion Beam Physics and Materials Research, PF 510119, D-01314 Dresden, Germany, private communication (2014).
- ⁶²G. H. Kinchin and R. S. Pease, *Rep. Prog. Phys.* **18**, 1 (1955).
- ⁶³M. J. Norgett, M. T. Robinson, and I. M. Torrens, *Nucl. Eng. Des.* **33**, 50 (1975).
- ⁶⁴M. J. Caturla, T. Diaz de la Rubia, and G. H. Gilmer, *Nucl. Instrum. Methods B* **106**, 1 (1995).
- ⁶⁵P. Arnolda, C. Inguimbert, T. Nuns, and C. Boatello-Polo, *IEEE Trans. Nucl. Sci.* **58**(3), 756 (2011).
- ⁶⁶M. Moll, E. Fretwurst, M. Kuhnke, and G. Lindstroem, *Nucl. Instrum. Methods Phys. Res., B* **186**, 100 (2002).
- ⁶⁷B. C. MacEvoy, G. Hall, and A. Santocchia, *Nucl. Instrum. Methods Phys. Res., B* **186**, 138 (2002).
- ⁶⁸K. Gill, G. Hall, and B. MacEvoy, *J. Appl. Phys.* **82**, 126 (1997).
- ⁶⁹G. Lindstroem, *Nucl. Instrum. Methods A* **512**, 30 (2003).